Chapter 3 : Experimental setups

This chapter is aimed to describe the two major experimental setups used for silicon detectors radiation hardness testing in Louvain-la-Neuve. First, the electrical test bench will be addressed and second, the irradiation setup around the intense fast neutron beam line. A third section will develop some peculiar aspects in the case of the CMS tracker sensors studies, such as the irradiation and test protocol. Additional equipment is presented in the annexes.

3.1. Electrical characterisation setup

The large amount of sensors and structures to be tested for irradiation qualification of the CMS tracker silicon microstrip detectors requires the use of an automatic test bench. This latter must be designed in order to perform a complete electrical characterization of a device with as less user interventions as possible. It also has to be flexible enough to cope with the several sensors designs and versatile enough to allow quick implementations of special measurements.

Among the measurements possible on a segmented semiconductor detector, CMS focuses on the macroscopic characteristics and functionalities: CV, IV, strip parameters like bias resistors, strip leakage current, coupling and interstrip capacitances, interstrip resistances. Besides these properties, common to all microstrip sensor designs and test structures, additional measurements like CV and IV on diodes, inspection of the oxide layer quality through a MOS capacitance measurement have been added to the program.

The following sections will first describe the setup and then give more details on some specific hardware-related problems before entering the details of the performances and the obtained measurement accuracy.

3.1.1. Instrumentation, acquisition program

In Louvain, the electrical test bench is built around a Karl SüSS PA-200 semi-automatic probe station (shown below on Fig. 30). An especially engineered chrome plated steel plate is placed on top of the chuck. It has thin vacuum grooves to maintain the device during the whole tests and movements and provides a good electrical contact to the backplane of the device.

The chuck is temperature-regulated by a cooling loop and additional peltier elements. Methanol, used as cooling fluid, is kept at low temperature (-5°C) by a Huber cooling plant located outside the probe station clean room. It is kept at a constant temperature whereas the peltier elements ensure the accurate temperature setting and stability. This system is able to cool the chuck down to at least –40 °C and heat it up to 100 °C.

The light-tight enclosure around the chuck is continuously flushed with dry air to avoid any condensation on the device under test during low temperature measurements.

The monitoring of the test environment is made via he use of an active relative humidity sensor and a passive Pt100 resistor housed in the chuck to read its temperature. Special care has been taken to the reading of this latter resistor as the cables used to connect it have an influence on the measurement itself due to their specific resistivity. A correction based upon the length of the cable has been introduced in the acquisition program.

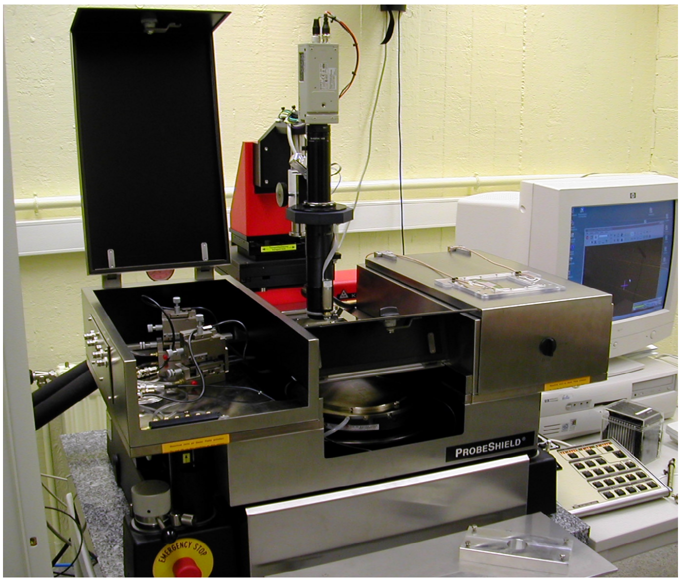

Fig. 30 : The semi-automatic Probe station.

Besides the biasing connection on the chuck (backplane contact, mentioned above), three needles and one additional (directly attached on the plate and pictured on Fig. 31) surround the device to ensure all the electrical connections required. The use of a probe card has been envisaged, but ruled out due to the many different designs to be handled by the same setup.

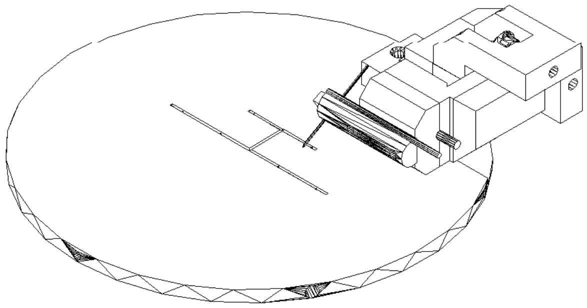

Fig. 31 : The lab-made chrome plated chuck and its fixed needle.

To permit an automated test sequence (composed of many different type of measurement), a switching matrix (cf. Fig. 32) is used to connect the needles to all instruments. Among these, the setup comprise a Keithley 2410 sourcemeter to bias the devices; a Keithley 6514 electrometer to accurately measure currents trough sensors, detect shorts and calculate the resistor's impedances; an Agilent 6614C low voltage source and a 4284 LCR to measure capacitors. This latter can be connected either directly to the needles using the switching matrix or trough a lab-made decoupling box to perform capacitance-voltage ramps, requiring the mixing of both the HV source and LCR measurement signal on the same needles.

The acquisition instruments, the probe station movements as well as the temperature of the chuck are all controlled by GPIB using a unique acquisition program, written under LabVIEW®. After a procedure meant to load the structure to be tested in the probe station (including pitch parameter calculation to allow the program to make accurate movements from strip to strip), the user interface allows choosing the measurement parameters (e.g. the ramping scheme) and the tests to be performed. The results are plotted at the end of each test and a separate file can be written on demand. Environment parameters such as temperatures or current position on the device are also shown.

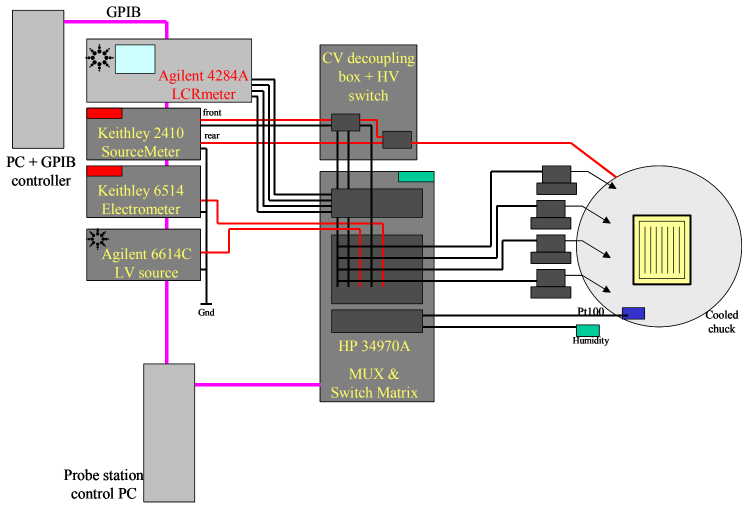

Fig. 32 : Schematic view of the instruments and electrical connections around the probe station.

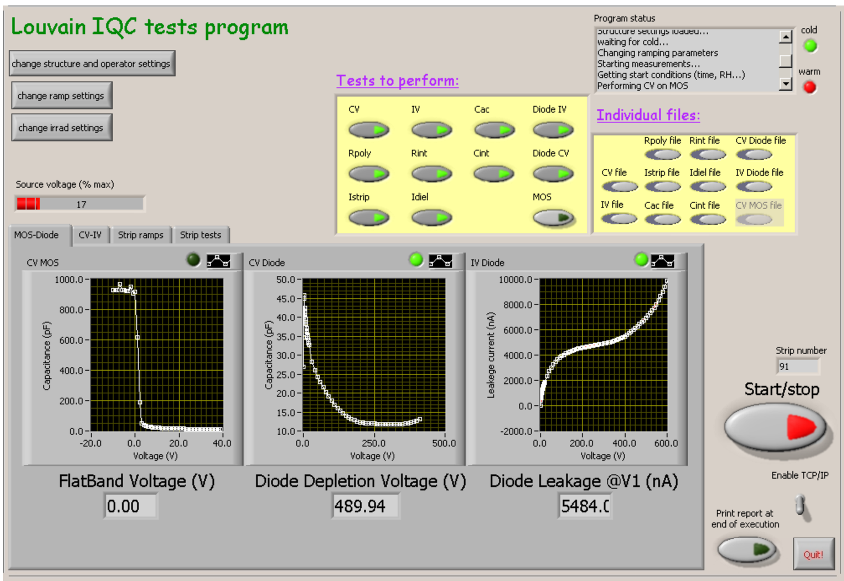

Fig. 33 : Screenshot of the probe station acquisition program.

Behind its main control panel (Fig. 33), this program is arranged in many different layers according to the level of the actions performed. The most basic commands are directly related to the instruments, and these commands are arranged in measurement routines, which are in turn used to perform the whole measurement of a parameter, including a curve fit in certain cases and the writing of the results in a dedicated file. These measurements are in turn arranged altogether to perform an entire test of all the common bulk and strip parameters.

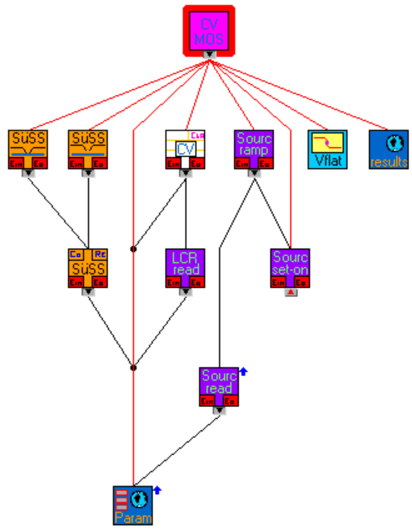

Fig. 34 : LabVIEW® program hierarchy in the case of a CV on MOS device.

Fig. 34 illustrates this organisation in the case of a CV measurement on MOS device in order to determine the flat band voltage. One can distinguish the probe station commands on the left, the measurement itself with the bulk capacitance measurement routine and the sourcemeter control, the calculus of the flat band voltage on the right, and finally the global variable used to store the results.

In the framework of the CMS IQC testing, the program is also used to load the measurements made before irradiation as well as the irradiation parameters (fluence, date, etc.) and format the results in a XML file whose format is suitable to be put in the CMS construction database.

3.1.2. Performances, measurement accuracy

The electrical characterisation setup is supposed to accurately measure very low currents. Indeed, the leakage current of a baby detector on a CMS test structure at –10 °C is of the order of a nanoampere and we also have to determine the value of resistances higher than 20 GΩ. Dealing with such low currents requires a good wire shielding and the avoidance of any ground loop in the circuitry.

As there is in fact no magical recipe to ensure a perfect insulation without any ground loop, we used some well-known ingredients such as shielded coaxial cables (to cope with the high voltage applied on the structures, these are able to sustain voltages up to 1000 V) and metallic boxes when lab-made circuits were to be built. The apparatus connections are as few as possible, to avoid loop generation, although ensuring each instrument is connected to the shielding lines in this way. Some of the sources and measurement devices have separate “common” and “chassis” connections to be used either to define the zero level between the instruments or to shield the setup, in the case of our electrometer, it has been found that one should disconnect the coupling of these connections to avoid perturbation of the current measurements.

On the switch matrix level, we realized also that the connection of all cable shields together is not a good method. Avoiding current parasites requires additional individual connections of the shields of the two cables connected through the matrix. We do not know exactly the reason of this as all of these were already connected together in the first scheme. This has however easily been achieved as each switch of the matrix is in fact doubled for this purpose.

Once these connections made, the accuracy and reliability of the current measurements were improved. The current measured on non-shorted silicon sensor dielectrics at 10 V are less than 1 pA. This could lead to interstrip resistance measurements up to 100 GΩ that would suffice for CMS testing (the acceptance criteria being 20 GΩ), but to ensure a higher precision and avoid perturbation due to higher post-irradiation leakage currents, the measurement is performed doing a small current-voltage ramp whose slope will give the resistance.

Beside the current measurements, the parasitic capacitance was also reduced to about 10 pF (12 pF in the case of the CV measurement because of the decoupling box). The LCR has a specific calibration routine to deal with additional stray capacitance, requiring the measurement of these capacitances in open and shorted contact configurations. Unfortunately, this very practical feature is useless in our case, as the switching matrix changes the stray capacitances for each type of measurement. However, we found that the stray capacitances values for our setup values are acceptable and can directly be subtracted from the measurement in order to obtain the relevant sensor value. This latter subtraction needs frequent calibrations of the system because the parasitics changes a bit during the maintenance of the system (e.g. needle changes).

Another effect of the setup on the measurements is due to the vacuum-induced strain on the structure. Indeed, this constraint can affect the leakage current* of a detector due to lattice deformations. This effect has been observed with many test setups and has been proven to be sensitive to the vacuum strength. This has been an issue for some centres among the sensor group as the problem could even lead to the rejection of sensor batches. These showed a high leakage current about 20 µA, but only when stressed by the vacuum applied on the sensor to maintain it on the chuck (Fig. 35).

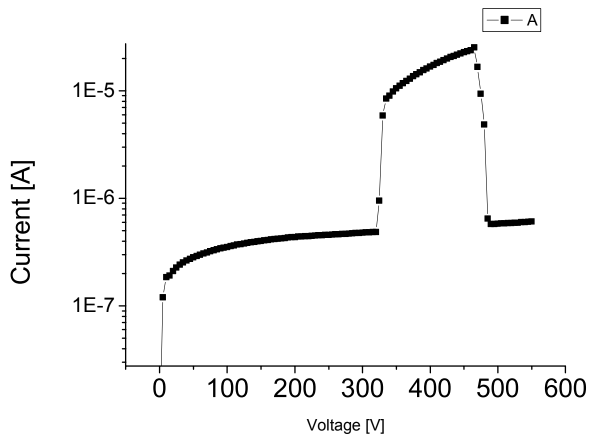

Fig. 35 : influence of chuck-vacuum in the Karlsruhe setup (the step in current appears when vacuum is applied on the sensor). This effect is observed despite the high planarity of the chuck plate. Taken from [47].

In our case, as already mentioned above, we use a dedicated chrome-plated plate on the chuck. It has been rectified to be as flat as possible and its vacuum grooves are only a millimetre wide. Fig. 36 shows clearly that vacuum has no effect on the measurement of the total leakage current of a sensor. The difference of vacuum behaviour is probably due to the vacuum strength and grooves design.

---

* The electrical resistivity of a semiconductor changes with strain, this is the principle of strain gauges, and hence on a reverse-biased sensor, a higher leakage current can be observed under strain. This is due to changes in electron and hole mobility with changes in crystal structure as strain is applied.

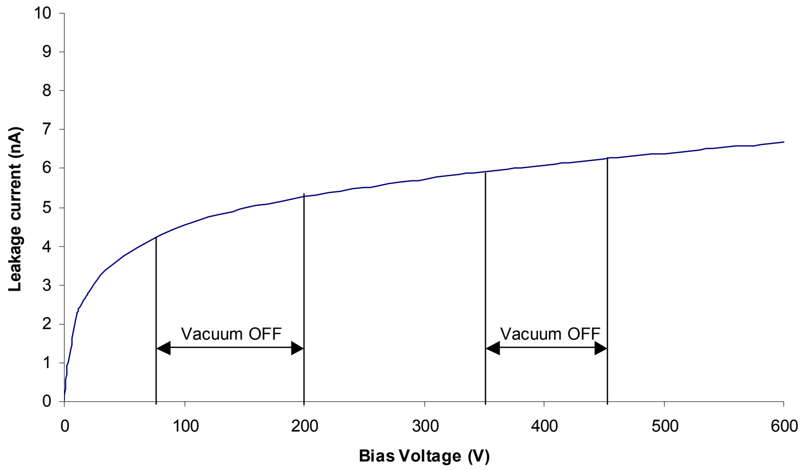

Fig. 36 : Effect of vacuum on Leakage current (measurement performed at 20 °C on non-irradiated 500 µm thick sensor). There is clearly no vacuum-induced effect.

3.1.3. Encountered Problems

Once the corrections for parasitic capacitances were implemented in the program, the most problematic issue encountered was the pinhole generation after irradiation.

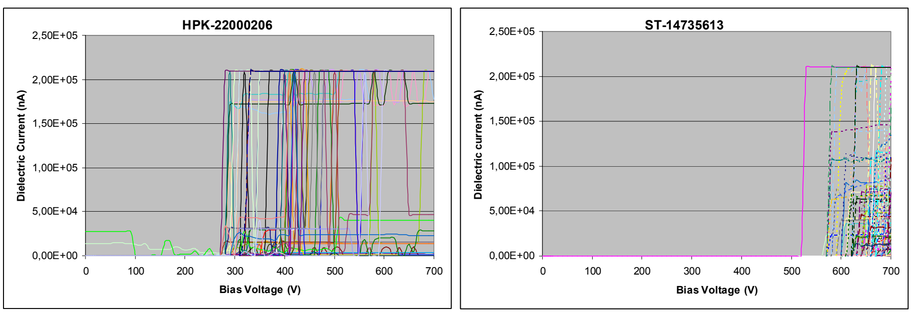

Fig. 37a, b : Dielectric breakdown observed on thin (HPK) and thick (ST) structures after irradiation. Both type of structures where submitted to the same test conditions, but Hamamatsu (HPK) devices are more affected due to lower dielectric breakdown voltage.

Most tested strips showed a breakdown in the dielectric current as a function of the bias voltage (cf. figures above). The Hamamatsu structures were most affected, as their oxide resistance to breakdown was lower than ST-manufactured ones. The switching scheme and test ordering was quickly suspected as the problem arose after the full integration of the tests within a single program sequence.

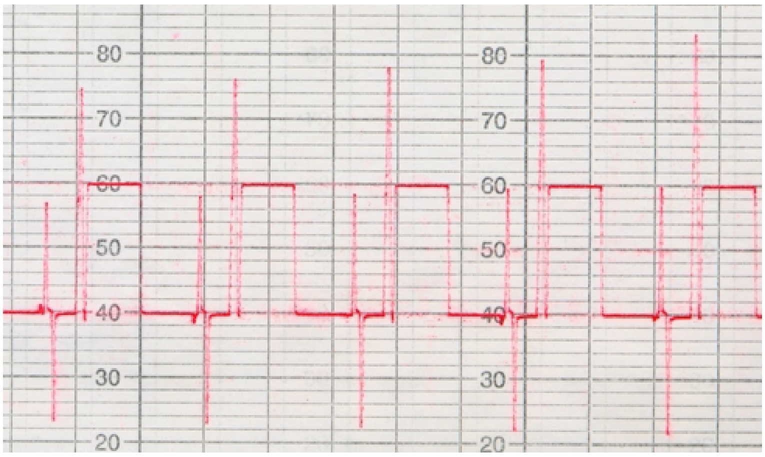

Fig. 38 : Voltage applied on the strip dielectric during 5 strip test sequences (before switching revision). The transient variations at each step were the cause of pinhole creation.

A direct measurement of the voltage applied to the strip dielectric during a strip test sequence rapidly pointed out the existence of parasitic high amplitude voltage peaks applied between DC and AC pads. These peaks (even bigger than shown on Fig. 38 due to the pen-tracer speed) have increasing amplitude with the bias voltage and were the cause of the observed breakdowns.

The solution was first to change the order of the strip parameter tests, minimising the number of switching needed and second, either to ramp the sensor down to 0 V between the strip to strip movements or to keep its bias ring connected at all times during the tests. It is evident that the latter option has been implemented to speed up tests.

Fig. 39 shows the impact of these changes on the voltage applied on the dielectric: the peaks have been removed and the pinholes have indeed stopped to appear in the post-irradiation measurements.

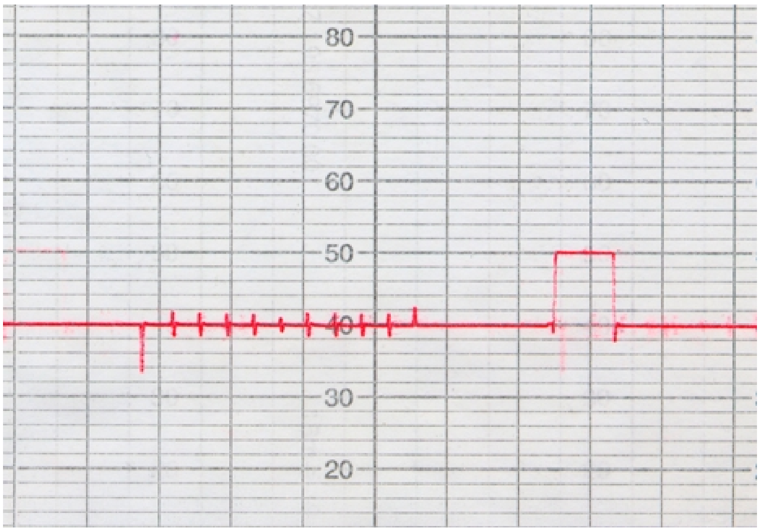

Fig. 39 : Voltage applied on one strip test sequence (after switching revision). Transient peaks have been removed, and setup-induced pinhole creation stopped.

The second problem, still arising sometimes, is bound to our CV-decoupling box. The circuitry of this filter is pictured, without the additional relays, on Fig. 40. The resistors (R_1 and R_2) going from the HV source to the backplane contact of the sensor have to undergo the whole sensor current. Under severe current breakdowns, these resistors may burn as their maximum power lies around 0.6 W. Since these resistors have values of 38 kΩ and 62 kΩ, this sets a limit on the sensor current at 3 mA, which is large enough for all devices irradiated (typical currents for test structures being 60 µA). We could have added diodes or changed the resistors for more power-tolerant ones but we did not as the burning of the resistor indicates that we are approaching the capabilities of our Keithley sourcemeter, limited to 10 mA. This was good as it prevents us from applying lower-than-expected biasing voltages to the detector under test.

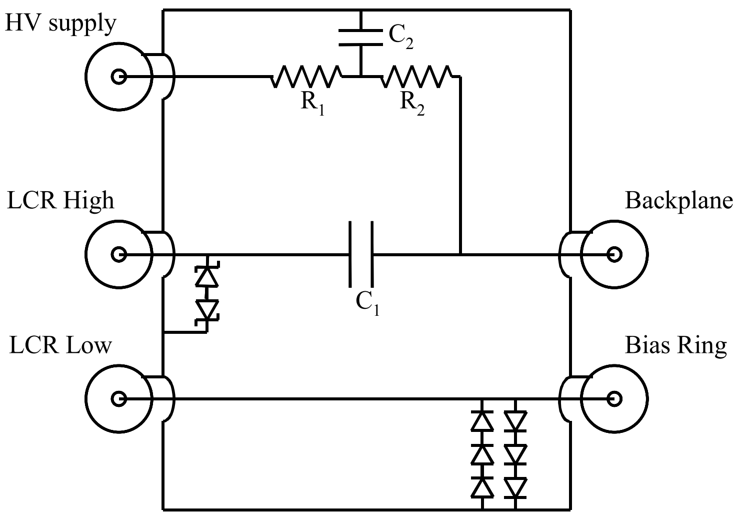

Fig. 40 : CV decoupling filter principle.

3.1.4. Cross calibration with the Karlsruhe system

Whereas the depletion voltage determination as well as the leakage current measurements did always show a good agreement between measurements made in Louvain and by our colleagues in Karlsruhe or even in institutes involved in the CMS sensor group, the strip parameters measurements did require further checks and setup modifications.

First, if the coupling capacitance measurement calibration has been performed easily because of their relatively high values (around 60 pF for a baby detector, more than 500 pF for most full size detectors) compared to the capacitance parasitic, the story was a bit different considering the interstrip capacitances. For a baby detector, these capacitances are of the order of 1 pF before irradiation. The comparison of our results (Fig. 41, below) showed a fairly similar behaviour of the interstrip capacitance-bias voltage curve with respect to the observed decrease and bumps, but with different values. One between the two setups could therefore be improved.

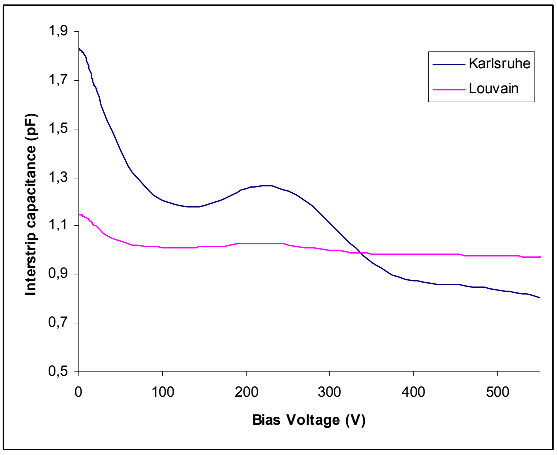

Fig. 41 : Interstrip capacitance measurements performed at Karlsruhe & Louvain, after irradiation on the same p-irradiated structures.

On the Louvain setup, we realised that the interstrip capacitance measurement was perturbed by the needle in contact on the AC pad. Indeed, measuring the small interstrip capacitance requires the LCR to work at high frequency (1 MHz in this case). At that frequency, the coupling capacitance is shorted (in red on Fig. 42, it is 2 orders of magnitude higher than the interstrip one, and has hence a very low impedance at 1 MHz) and the AC pad needle is hence connected to the measuring needles, perturbing the measurement.

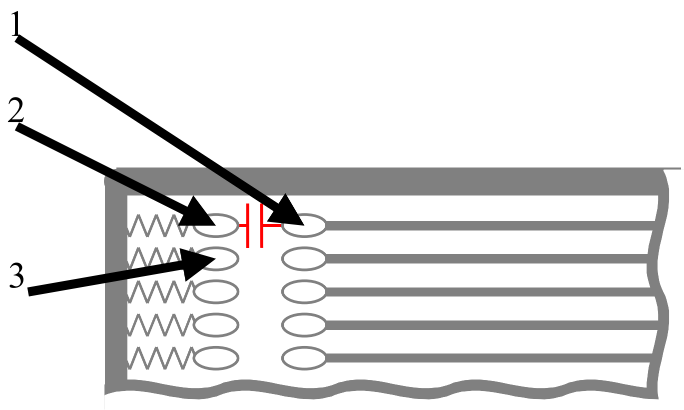

Fig. 42 : Interstrip capacitance measurement perturbation.

The problem has been solved by also connecting Fig. 42's needle 1 together with needle 2 at the level of the switch matrix, hence not only using needles 2 and 3 during the measurement, but also the last other needle in contact with the pads.

The new measurement scheme gave values between 0.66 and 0.68 pF for baby detectors, 2.33-2.35 for OB2 sensors (all measurements performed at full bias, before irradiation). The ratio between these measurements is 3.5. Using the usual capacitance approximation formula (3.3), the interstrip capacitances should be proportional to the strip lengths and inversely proportional to the strip pitches. This leads to a ratio R of 3.9, slightly different from the observed one, but this approximation does not take the capacitance border effect into account and these have an impact on the strip capacitances.

$$C = \frac{2\varepsilon_0 S}{d} \tag{3.1}$$

$$R = \frac{L_{strip,full}\, pitch_{baby}}{pitch_{full}\, L_{strip,baby}} \tag{3.2}$$

On the other hand, the Louvain setup gives now the same interstrip capacitance values than the Karlsruhe setup.

Another measurement that appeared to be tricky in the beginning was the determination of interstrip resistances. Indeed, the measurement of resistors as high as several GΩ implies the accurate measurement of very low currents. As mentioned above, the currents measured with our setup on non-shorted silicon sensor dielectrics at 10 V are less than 1 pA, but due to the high sensitivity of the measurement to any perturbation, the connections evolved a bit to cope with the high leakage current of the detector after irradiation. Fig. 43 shows interstrip resistance measurements as a function of the bias voltage. These measurements are both made in Louvain and Karlsruhe on a standard test structure. The continuous red lines show the min. and max. measurements made in Karlsruhe (on the same structure but at a different annealing stage). This figure clearly shows that both setups give similar results.

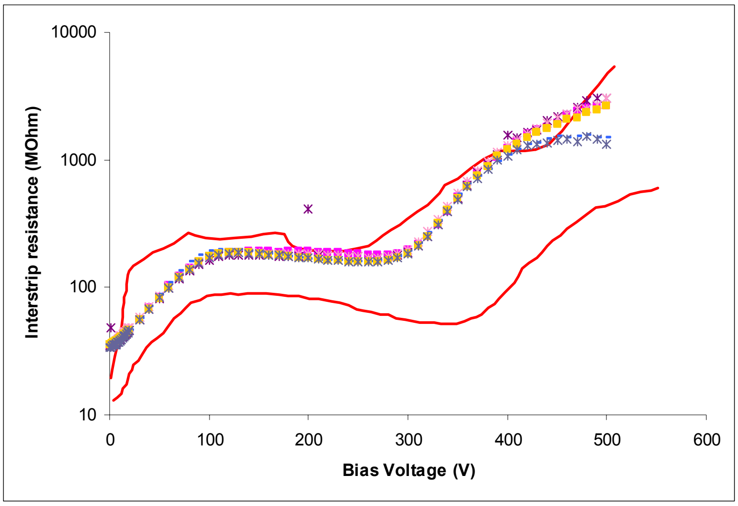

Fig. 43 : Post-irradiation interstrip resistance measurements made in Louvain and Karlsruhe (on the same structure but at a different annealing stage).

At this stage, both CMS-IQC setups within the sensor group were giving consistent results.

3.2. The T2 beam line and instruments around the irradiation zone

This section consists of a detailed overview of the neutron beam line and the experimental setups around the irradiation zone. The first part of this section is largely inspired from ref. [48]. This latter being largely devoted to the neutron beam, it will only briefly be introduced here. Some of the details of its monitoring are also further developed in the annexes.

According to the irradiation protocol, the environment in the irradiation zone has to be as close as possible to the CMS tracker environment, described in sections 1.2.2.

In that sense, and first of all, one cannot neglect the low temperature requirement, mandatory not only to match the Tracker atmosphere, but also to avoid uncontrolled annealing effects during irradiation. This temperature requirement comes with a stringent condition on the relative humidity inside the irradiation cold box to ensure there will be no condensation on the sensors.

Second, sensors should better be biased during irradiation. This is a very demanding requirement because of the high irradiation rate and charged particle levels in beam or reactor radiation fields. It also explains why there is no extensive study of the influence of biasing during irradiation on the radiation damage parameters of silicon sensors. On this aspect, a great asset of our neutron beam, compared to proton beams or other radiation sources, is that its low gamma and charged particle contamination permits the biasing up to voltages as high as 650 V and even more in the case of CMS structures, keeping the device fully depleted during the entire test[*]. The influence of biasing during irradiation is discussed in section 2.3.5 and further developed in 4.2.1.

Finally, the PC-based control of the power supplies is also used as an input to an acquisition program logging all the irradiation parameters during and also after the irradiation period.

3.2.1. The High flux neutron beam line

The high flux neutron beam, especially designed for LHC radiation hardness tests, uses a primary 50 MeV deuteron beam to produce neutrons from the $^{9}Be(d,n)^{10}B$ reaction. It has been shown that this reaction has the highest neutron production cross section at 50 MeV compared to other reactions like $^{7}Li(p,n)^{7}Be$. As the deuteron beam optics may slightly vary along the different tests, a Titanium collimator (pictured in Fig. 44) is used to define the beam spot on the ^{9}Be target and hence keep the neutron beam geometry constant. The production target is made of a Beryllium cylinder with a thickness of 2 cm and a radius of 4 cm. It is encased in a water-cooled copper ring that is electrically insulated from the rest of the beam line. In this way, the deuteron current can directly be read on the target for monitoring purposes.

To keep the charged particles and gamma contaminations as low as possible, a special filter is placed right after the production target. It is made of a 1cm thick polyethylene slab stacked together with 1mm of Cadmium and 1mm lead. The aim of this filter is not only to remove most of the charged particle contamination, but also to absorb part of the gamma produced and to harden the neutron spectrum by removing its low energy part.

---

[*] Without any annealing, the depletion voltages of typical CMS structures can rise up to 600 V when reaching the nominal LHC fluence.

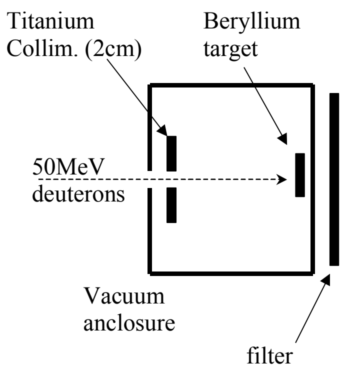

Fig. 44 : Neutron production in the T2 beam line.

An extensive study of the beam properties has been carried out in the past (cf. [48] and [49]), using several dosimetry techniques to determine the beam spatial extension as well as its energy spectrum and other particle contaminations. The most important features are outlined below.

First, the neutron energy spectrum, determined using several different activation foils (cf. A.1.2 for a description of the method) is shown in Fig. 45. In the context of the CMS sensors tests, we compute a hardness factor to convert the real fluence into 1-MeV equivalent fluence according to equations (2.9) to (2.11) and using factors taken from references [41] and [42]. In this case, the obtained hardness factor is 1.95.

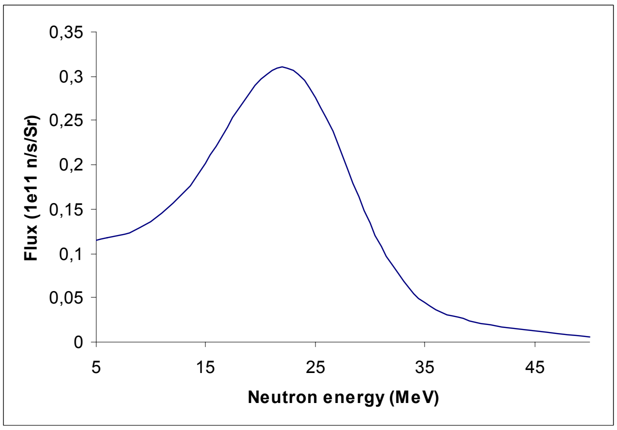

Fig. 45 : The fast neutron beam line energy spectrum. Taken from [49].

Then, the neutron yield and dose rate have been measured using three methods: a calibrated ionization chamber mounted together with a polystyrene phantom, RPL dosimeters and alanine dosimeters. The integrated neutron yield is 6.6 10^{11} neutrons/µC/Sr. For 10 µA of deuteron current on the target and at a distance of 9 cm from this latter, this yield corresponds to a neutron flux about 7.3 10^{10} n/cm^{2}s at the centre of the beam. Fig. 46 gives the radial extension of the beam as a function of the distance from the target, a useful function to determine the position of the samples to be irradiated.

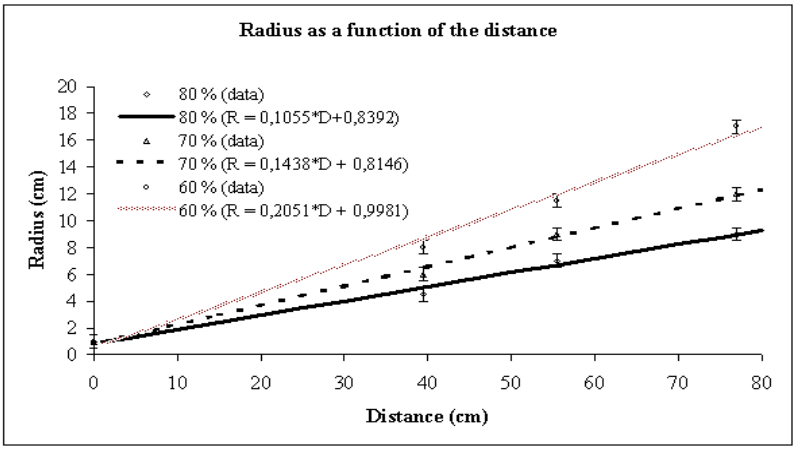

Fig. 46 : Radial extension at 80, 70 and 60 % maximum of the T2 neutron beam line, taken from [49].

Finally, the beam contaminations have been assessed using Monte-Carlo simulations because these are rather difficult to measure. The results of these simulations are shown in Table 7.

Particle type	Fraction (% of neutron yield)	Average energy (MeV)	Maximum energy (MeV)
Proton	0.015	12.61	25
Electron	0.016	1.57	6
Gamma	2.4	1.93	10

Table 7 : The high flux neutron beam contaminations.

3.2.2. Sensor environment, cold box

As mentioned at the beginning of this section, irradiations of silicon sensors have to be performed in a dry and cold environment. To fulfil this requirement, we equipped the neutron beam line with a temperature regulation system that also ensures a low relative humidity within the cold box.

Depicted in Fig. 47, the cooling principle is pretty simple: a proportional gauge, controlled by a PID regulator*, is used to regulate airflow. This latter is further dried using silica gel bottles and thereafter cooled by liquid nitrogen. The mixing of dry air and evaporated nitrogen ensures a very low relative humidity. Once cooled, the air flows to the irradiation box through insulated pipes. The temperature inside the cold box is measured using a Pt100 sensor that is directly read by the PID regulator. The regulation can be switched off or bypassed using the manual gauge mounted in parallel to the proportional one.

Several different cold boxes have been used as the irradiation setup was improved. All of these were made of 6 cm thick insulating walls, with opaque-Mylar windows on the beam entrance.

A calibration and performance test has been performed with the first cold box (inner volume of 18 l). Temperature has been monitored using an additional Pt100. Fig. 48 shows the temperature evolution, starting with the automatic calibration setup procedure. From this measurement, it can be seen that the calibration of the cold box takes about 30 minutes, but this result is highly dependant on the volume of the cold box and on the initial temperature of the cooling system. A more interesting result is the temperature stability, assessed by the maximum deviation in a stable temperature plateau, which is less than 0.5 °C and hence well suited for our purposes. Fans placed inside ensure the temperature uniformity within the box.

---

* PID stands for Proportional-Integral-Derivative: the command signal of the regulating unit depends not only on the gap between the parameter setup and the measured value, but also to its time dependence. An introduction to PID regulation and the automatic setup procedure of the yokogawa unit can be found in [28] and [50].

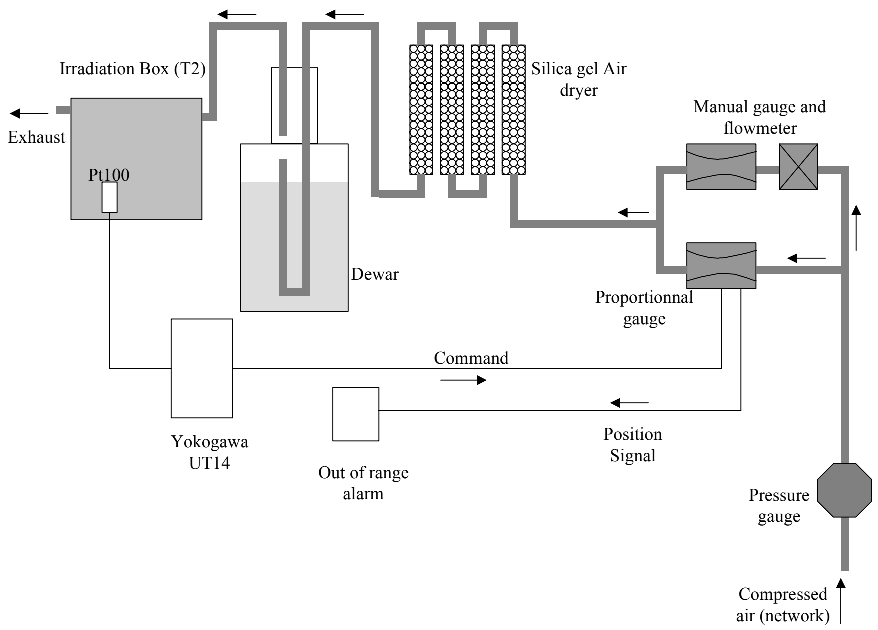

Fig. 47 : Principle of operation of the irradiation cooling system.

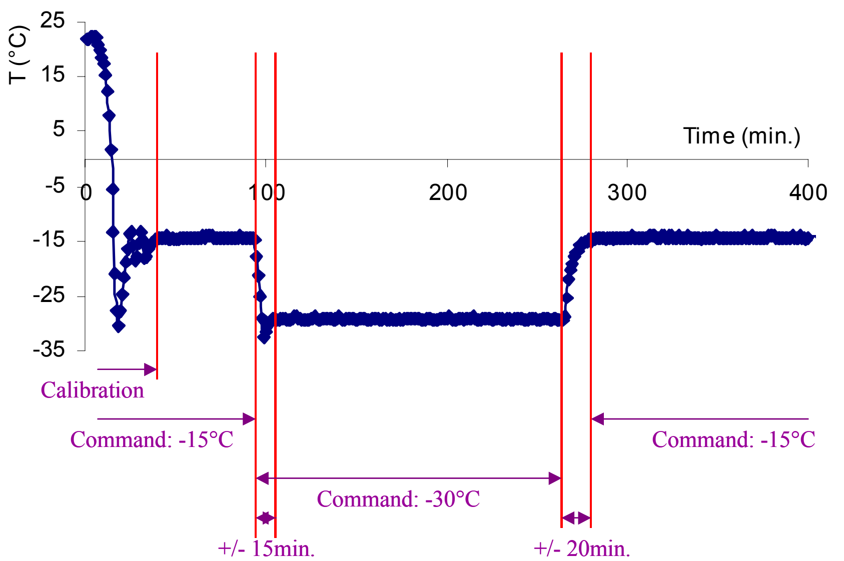

Fig. 48 : Time evolution of the temperature inside the irradiation cold box during calibration setup and afterwards.

Beside the temperature criteria, the relative humidity inside the irradiation box is another important feature of the system. Indeed, the box is unusable if the dew point is so high that condensation occurs on the sensors. First measurements of the relative humidity were a bit disappointing: the remaining relative humidity was about 30 % at -10 °C, with a corresponding dew point of –16 °C that is way too close to the irradiation temperature of –10 °C. A new cold box solved the problem: a better air tightness reduced exchanges with the ambient air and lowered the relative humidity down to 4 % at –10 °C (dew point = -40 °C).

A major drawback of this system is the maintenance of the silica gel air dryer, to be performed once or twice a year depending on the use.

Fig. 49 shows a picture of the irradiation setup equipped with the latest cold box on its sliding rail. This latter allows the irradiation of 3 different stacks of sensors (cf. next paragraph) without opening the irradiation zone. This saves time and optimises the use of the allowed beam time as the radiation level inside the irradiation zone quickly increases after the beginning of the irradiation and as several hours of cool down are necessary to penetrate it again. The movement of the box is made using cables running out of the irradiation zone. Also shown on the picture, the high voltage electrical connections used to bias the sensors.

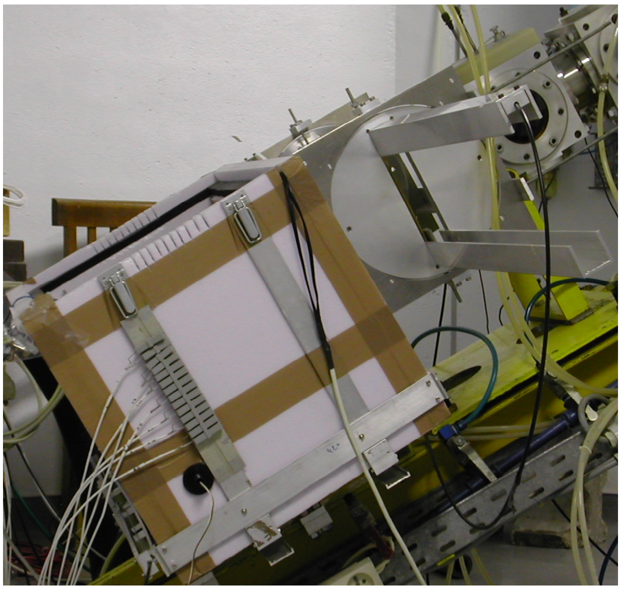

Fig. 49 : Fast neutron beam line irradiation box on it’s sliding rail. One can distinguish the HV connections for sensor biasing on the side.

3.2.3. Sensor biasing

Having addressed the issues about the irradiation environment, we are coming now to the sensors themselves. There's no need to say that these will be biased during their operation in the CMS tracker and hence, the opportunity to bias the sensors during irradiation is an asset when considering radiation hardness tests, even if there is no study yet on the impact of High voltage on the sensor's radiation hardness. This opportunity has already been discussed from the neutron beam radiation environment point of view and the considerations on power supplies and connectivity of the sensors are addressed in this paragraph.

First, an estimation of the current drawn by the silicon sensors during irradiation can be obtained with the alpha parameter before annealing, known from literature (e.g. [32]), the volume of the device under test (if fully biased) and the 1-MeV equivalent fluence attained during irradiation. As discussed in section 2.3.3, this estimation is calculated using equation (3.3).

$$I_{leakage} = V_{device} \alpha_0 \Phi_{1-MeVequivalent} \qquad (3.3)$$

For CMS test structures and sensors, the leakage currents computed in this way are listed in Table 8 and Table 9 for fluences of 10 and 15 years of LHC operation, and at room temperature.

The average leakage current to be expected on full size sensors is 42 mA (69 mA maximum) at 15 years LHC fluence. For test structures, the average value is 0.19 mA (0.25 mA maximum). As mentioned above, the values are quoted for sensors at room temperature and as irradiations are performed at –10 °C, the currents drawn by the devices will be about 16 times lower (5 mA max.).

Sensor type	Leakage current at 1.6 10^{14} n/cm^2 (mA)	Leakage current at 2.4 10^{14} n/cm^2 (mA)
IB	34,7	52
W 1 tec	30,6	45.9
W 1 tid	40,9	61.4
W 2	46.6	69.9
W 3	38.4	57.6
W 4	35.8	53.8
Test structure	0.16	0.24

Table 8 : Leakage currents foreseen for 320 µm CMS structures and sensors.

Sensor type	Leakage current at 0.5 10^{14} n/cm^2 (mA)	Leakage current at 0.8 10^{14} n/cm^2 (mA)
OB	20.4	32.7
W 5a	19.9	31.9
W 5b	17.4	27.9
W 6a	20.4	32.7
W 6b	20.2	32.3
W 7a	19.3	31
W 7b	17.7	28.3
Test structure	0.08	0.13

Table 9 : Leakage currents foreseen for 500 µm CMS structures and sensors.

Now that the foreseen leakage current is known, the depletion voltage at end of the irradiation has to be computed. It can be done using the Hamburg model discussed in 2.3.3. This latter has to be given the initial effective doping concentration, extracted from CV measurement (using (3.4) that takes the effect of the segmented geometry into account, cf. [26]), and the 1-MeV equivalent fluence reached. The other parameters of the model such as donor removal constants will be taken from literature. In this case, we do not have to discuss about any reverse annealing as the irradiation is performed at low temperature. This leads to a simplified formula shown in (3.5), where only the donor removal, stable damage and beneficial annealing (at t=0) terms are taken into account.

$$\left|N_{eff}\right| = \frac{2\varepsilon\varepsilon_0}{qd^2}\left(\frac{V_{dep}}{F_{geom}} + V_{bi}\right) \qquad (3.4)$$

$$\left|N_{eff,after}\right| = \left|N_{eff,before} - r_c N_{eff,before}\left(1 - e^{-c\Phi_{1-MeV}}\right) - \Phi_{eq}\left(g_c + g_a\right)\right| \qquad (3.5)$$

The results shown below in Table 10 and Table 11 were obtained for an initial depletion voltage of 160 V and using a donor removal constant r_c of 0.8, which has proven to be a bit over-estimated in the case of our neutron beam (cf. 4.2).

Sensor type	Depletion voltage at 1.6 10^{14} n/cm^2 (V)	Depletion voltage at 2.4 10^{14} n/cm^2 (V)
IB 1	474	716
IB 2	521	781
W 1 tec	492	740
W 1 tid	492	740
W 2	527	789
W 3	545	814
W 4	526	788
Test structure	521	781

Table 10 : Depletion voltages foreseen for CMS test structures and sensors from the inner tracker (320 µm thick sensors).

Sensor type	Depletion voltage at 0.5 10^{14} n/cm^2 (V)	Depletion voltage at 0.8 10^{14} n/cm^2 (V)
OB 1	126	223
OB 2	145	249
W 5a	130	229
W 5b	134	235
W 6a	142	245
W 6b	132	231
W 7b	134	234
W 7a	139	241
Test structure	125	223

Table 11 : Depletion voltages foreseen for CMS test structures and sensors from the outer tracker (500 µm thick sensors).

According to these estimations, the average depletion voltage to be expected on full size sensors is 484 V (814 V maximum) at 15 years LHC fluence. For test structures, the average value is 502 V (781 V maximum).

Once combined with the leakage current results, the requirements on the power supply for the full size sensors are 1000 V with a current of 5 mA at least (80 mA if we want to be able to bias the sensors at room temperature and keep the system versatile). The biasing of baby detectors puts less stringent requirements (800 V at less than 1 mA), but on more channels as most of the radiation hardness study will be done using these test structures.

To match these requirements, we equipped the irradiation area with two Iseg High current power supplies (one channel each with 60 mA at 1 kV) and two CAEN N470 modules providing eight lower current channels (up to 3 kV at 1 mA). The Iseg power supplies are powerful enough to keep all sensors but W1tid and W2 (the most demanding sensors) biased at room temperature.

Many different options were considered to apply the biasing voltage to the sensors and test structures. Among these, only the use of bonding has proven to be satisfactory, as the other techniques (e.g. the use of needles) did not provide reliable electrical connection of the device to the high voltage cable. A sketch of the irradiation support plate dedicated to test structures is shown in Fig. 50. The electrical connection of the baby sensor is made on its side using two aluminium plates that are in turn connected to the high voltage cables. The design of the sensor plates is fairly similar. Another advantage of bonding compared to other solutions is the smaller spacing between the different plates of the irradiation stack. This leads us to considerations about the irradiation uniformity across a stack of supports. The sensors spacing is about 1.1 cm. This is less than the spacing obtained with any of the other solutions envisaged (e.g. conductive rubber). Using the beam specifications described above and at the usual distance from the target for CMS sensor irradiations, the spread around the mean fluence of a stack comprising 6 detector layers is ± 6 % (the biggest and lowest fluences at extreme positions of the stack are different to the middle one by 6 %).

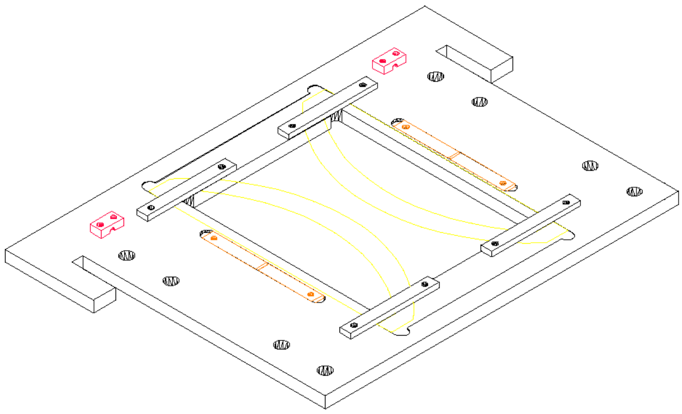

Fig. 50 : Irradiation support for the test structures. One can distinguish the aluminium strips on the side for bonding and electrical connection of the bias line and backplane of the sensor.

3.2.4. Acquisition and monitoring

The monitoring during irradiation is twofold: monitor the sensor bias but also the environment and the beam current. These tasks are ensured by a TestPoint® program reading a multichannel acquisition card and a Caenet interface card, also used to control the N470 HV power supplies.

On one hand, the CaeNET® controller reads the voltages and currents applied on the test structures and, on the other hand the acquisition card reads the analogue outputs of the Iseg power supplies (voltage and current) as well as those of a controller (used to read the temperature with a Pt100 sensor) and a current digitizer used to monitor the deuteron beam current (cf. A.1.1).

This program gives an online estimation of the integrated beam current, plots the irradiation parameters and stores these latter in a log file for further access. A screenshot of its user interface is shown below.

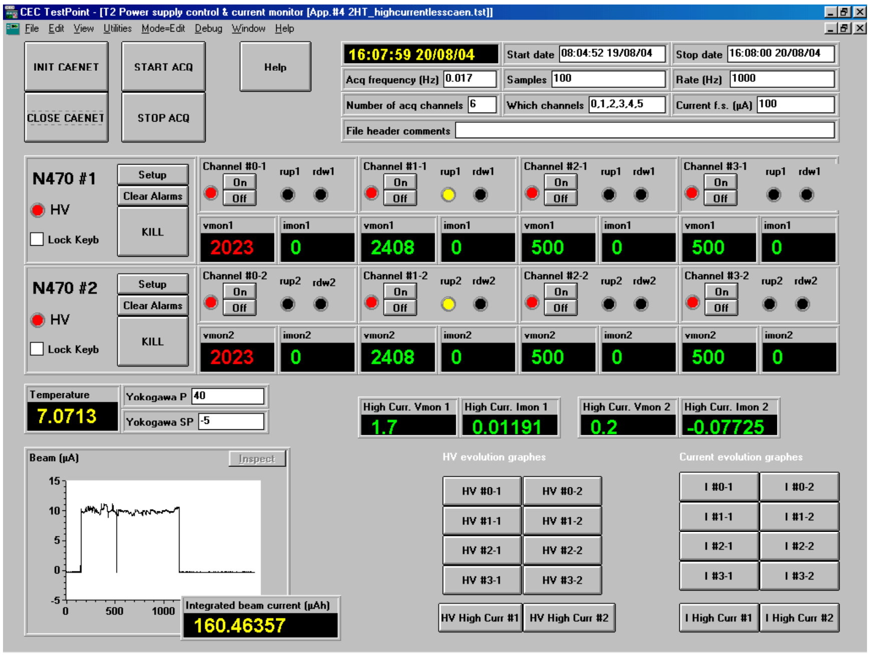

Fig. 51 : Screenshot of the irradiation monitoring program.

3.3. Sensor test protocol in Louvain

The tests performed during the last four years in Louvain are part of the overall CMS tracker sensor QA scheme, discussed in paragraph 2.5 and published in Ref. [45]. As an Irradiation Qualification Centre (IQC), Louvain regularly receives sensors and test structures from the QTC (qualification test center). At the production level, these sensors are labelled according to their type, manufacturer and production date but are also dispatched in "sets" by the QTC. Here is what happens to these sets when these arrive in Louvain (cf. Fig. 52).

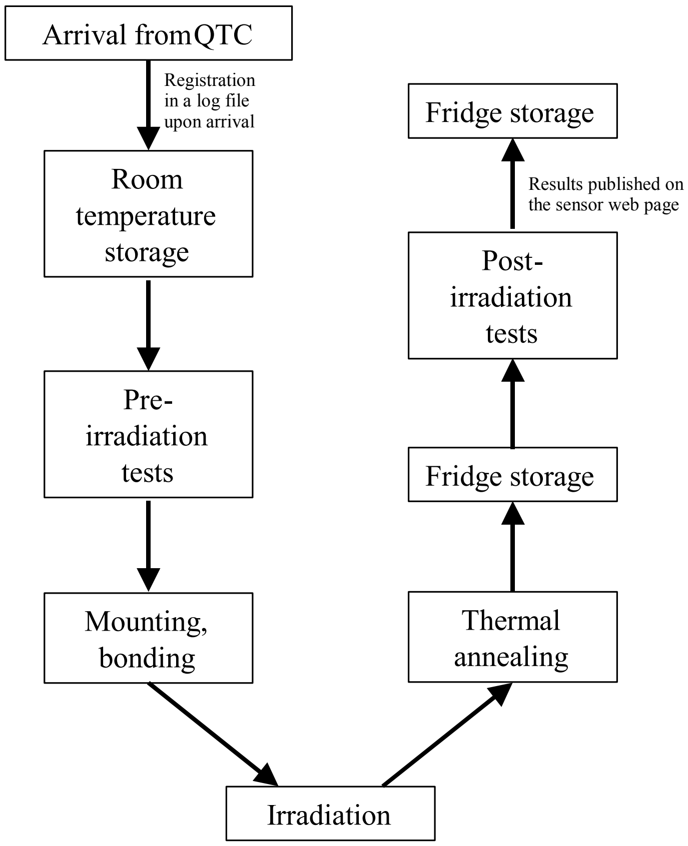

Fig. 52 : The sensor test protocol in Louvain-la-Neuve.

The pre-irradiation tests involve the usual CV, IV and strip parameter measurements, the latter being measured on one strip as a function of the biasing voltage and on several strips at a reference voltage of 400 V. A CV test on MOS device (in the case of test structures only, as sensor do not have MOS devices) has been added to the measurements on the baby detector. This has been decided because of high flat band voltages observed on ST structures in 2002*. The poor quality of the oxide (trapped charges) has some

* There were, in that time, several batches of ST sensors presenting a poor quality of the surface oxide, reflected by a high flatband voltage measured on MOS devices.

impact on the proton radiation tolerance of the devices, although no effect has been observed about the neutron radiation hardness. Before the irradiation, as well as after, all the tests are done at –10 °C.

After irradiation, the devices should be kept cold to avoid any uncontrolled thermal annealing. On the other side, avoiding condensation on the detectors requires them to be at room temperature during the manipulations. These operations should therefore be performed as quickly as possible.

The thermal annealing is performed with our lab-made oven (cf. A.2) for 80 minutes at 60 °C. According to previous studies on the evolution of the leakage current, this is equivalent to 14 days at room temperature. As this annealing procedure is a standard practice in the silicon community, we are able to compare the results obtained with CMS devices to other ones. A little stay of at least 8 h in the fridge after annealing is required to avoid the perturbation of the measurement by temperature-activated bistable defects [43].

When the detectors are ready to be tested again with the probe station, the same tests than before irradiation are performed (excepted the MOS test which does not give any good result because of the high density of trapped charges in the oxide). The program itself then makes a comparison of the strip parameters before/after irradiation and we check the evolution of the bulk parameters against the predictions of the Hamburg model (depletion voltage) and empirical results on the leakage current. For the ease of use in the community, a summary is published on the group webpage for each PQC set.

Afterwards, the sensors are kept in the fridge in case we need to perform further tests.

3.4. Summary

Before the start of this work, it was barely possible to perform the irradiation of silicon sensors in Louvain-la-Neuve. Indeed, the neutron beam was the only element available. We therefore started to equip the irradiation zone with cooling, biasing and monitoring device. The laboratory is now in possession of every adequate device useful to perform an irradiation in a controlled environment with respect to sensor bias, temperature and relative humidity. In the annexes, the required associated dosimetry methods are described as well as their calibration in this specific context.

The most complex system developed was the electrical characterization setup. The measurement of very low currents and determination of high resistances, the accurate assessment of small capacitances and the handling of high voltage requires the use of selected materials and components. The setup has been build step by step, integrating the different measurements together in a program able to perform a complete characterization in an automated way, including the temperature control of the chuck and the automation of the movements enabling to scan the sensor over its surface.

This setup required some iterations and debugging in order to gain confidence in the obtained results. Measurements on test devices and cross-comparison with other laboratories gave us that confidence.

Finally, a standard procedure for structure and sensor handling in Louvain-la-Neuve has been developed, so that all irradiations are performed in the same conditions.